

OSI: One-step Inversion Excels in Extracting Diffusion Watermarks

Yuwei Chen^{1,2} Zhenliang He^{1,2}  Jia Tang^{1,3} Meina Kan^{1,2} Shiguang Shan^{1,2}

¹State Key Laboratory of AI Safety, Institute of Computing Technology, CAS, China

²University of Chinese Academy of Sciences (CAS), China

³School of Information Science and Technology, ShanghaiTech University, China

{yuwei.chen, jia.tang}@vipl.ict.ac.cn {hezhenliang, kanmeina, sgshan}@ict.ac.cn

Abstract

Watermarking is an important mechanism for provenance and copyright protection of diffusion-generated images. Training-free methods, exemplified by Gaussian Shading, embed watermarks into the initial noise of diffusion models with negligible impact on the quality of generated images. However, extracting this type of watermark typically requires **multi-step diffusion inversion** to obtain precise initial noise, which is computationally expensive and time-consuming. To address this issue, we propose **One-step Inversion (OSI)**, a significantly faster and more accurate method for extracting Gaussian Shading style watermarks. OSI reformulates watermark extraction as a learnable sign classification problem, which eliminates the need for precise regression of the initial noise. Then, we initialize the OSI model from the diffusion backbone and finetune it on synthesized noise-image pairs with a sign classification objective. In this manner, the OSI model is able to accomplish the watermark extraction efficiently in only one step. Our OSI substantially outperforms the multi-step diffusion inversion method: it is 20× faster, achieves higher extraction accuracy, and doubles the watermark payload capacity. Extensive experiments across diverse schedulers, diffusion backbones, and cryptographic schemes consistently show improvements, demonstrating the generality of our OSI framework.

1. Introduction

The rapid advancement of diffusion models has catalyzed the emergence of numerous high-quality image generation platforms [35, 41, 44], significantly enhancing creative capabilities in both professional and consumer domains. However, the risks related to intellectual property, authorship, and accountability have also been increasing concurrently. Therefore, it is imperative to develop technical mechanisms to safeguard the copyrights of synthesized images and trace their unauthorized usage.

 Corresponding author.

Over the past years, digital watermarking has proven to be an effective mechanism for image protection and provenance [2, 5, 45]. In the generative era, watermarking remains a promising countermeasure for safeguarding diffusion-generated images, especially because the watermarking mechanism can be deeply integrated into the generation process. Training-free methods [47, 49] have emerged as one of the most promising paradigms for diffusion watermarking. These methods embed watermarks into the initial noise of diffusion models, which has a negligible impact on the quality of the generated images since neither the model parameters nor the generation procedure are modified. As a result, training-free approaches have become an active research focus and have undergone numerous refinements [6, 9, 15, 26–28, 34, 48, 50–52].

Despite the promise of training-free watermarking, representative methods such as Gaussian Shading [49] rely on **multi-step diffusion inversion** to extract watermarks, which incurs substantial computational overhead, particularly for large-scale deployment. A crucial asymmetry has been overlooked: while multi-step diffusion inversion can recover the *exact value* of the initial noise, the watermark extraction task is only concerned with the *discrete signs* of the noise. Therefore, we argue that adopting multi-step diffusion inversion for extracting Gaussian Shading style watermarks is “using a sledgehammer to crack a nut”, which introduces unnecessary computational complexity and latency. In other words, we believe that there exists a simpler and more efficient solution for watermark extraction. Notably, recent studies have developed one-step diffusion generation methods [13, 14, 33], which significantly reduce the computational cost of the image generation process. Conversely, *is it possible to develop a one-step inversion approach specialized for efficient watermark extraction?*

Based on the above analysis, we suggest that the extraction of Gaussian Shading style watermarks is more appropriately formulated as a *discrete classification* problem rather than a *continuous regression* problem. Accordingly, we propose **One-step Inversion (OSI)** framework, which

extracts a watermark through a single forward pass. Specifically, we first initialize the OSI model from the diffusion backbone to leverage its inherent capability of exact noise inversion [15, 43, 49]. Next, we construct a supervised dataset by using a diffusion pipeline to synthesize noise-image pairs. Finally, we finetune the OSI model on these data pairs with a sign classification objective, resulting in a one-step model for watermark extraction. In this manner, we achieve significant improvements in watermark extraction compared with previous multi-step diffusion inversion method, specifically: 1) a $20\times$ increase in extraction speed, 2) improved extraction accuracy, and 3) a double increase in watermark payload capacity. Furthermore, extensive experiments across diverse schedulers, diffusion backbones, and cryptographic schemes consistently show improvements, demonstrating the generality of our OSI framework. These properties make OSI a practical and promising approach in real-world deployment.

2. Related Works

2.1. Finetuning-based Diffusion Watermarks

Finetuning-based diffusion watermarking methods are intrinsically tailored to the diffusion architecture. A representative group of approaches update parameters within the original generation pipeline: WatermarkDM [53] trains the diffusion model on specially watermarked image datasets, and Stable Signature [12] finetunes the decoder to embed watermarks during latent decoding. Other approaches integrate auxiliary learnable modules: AquaLoRA [11] attaches learnable LoRA [22] to the diffusion UNet to embed watermark, and ROBIN [23] learns additional watermark parameters and learnable conditioning signals to modify intermediate sampling steps. Since these finetuning-based methods intervene in the generation process, they require careful balancing of training objectives, schedules, and parameterization to avoid severely degrading image quality.

2.2. Training-Free Diffusion Watermarks

Training-Free methods embed a watermark into the initial noise, thereby avoiding any modification to the diffusion model. These approaches can be broadly grouped into two families: frequency-domain watermark (Tree-Ring style) and spatial-domain watermark (Gaussian Shading style).

Tree-Ring Style watermarks Tree-Ring [47] embeds watermarks by *modifying the frequency statistics of the initial latent*, imposing concentric ring patterns that can be extracted via multi-step diffusion inversion. Although the generator remains training-free, such frequency-domain perturbations deviate from the Gaussian prior and may reduce image fidelity. Subsequent works [9, 26, 52] refine the frequency patterns to better align with the prior distribution,

aiming to reduce the perceptual impact while preserving watermark robustness.

Gaussian Shading Style watermarks Gaussian Shading (GS) [49] introduces a widely adopted spatial-domain paradigm. It bridges diffusion and cryptography by applying *sign masks* derived from the watermarks to control the signs of the initial latent, which is equivalent to *assigning a fixed subset of the latent space to each watermark*. GS employs repetition codes (REP) to enhance the robustness of watermark. PRCW [15] extends GS framework with pseudo-random error-correcting codes (PRC) [8] to enhance undetectability. A series of follow-up studies [6, 27, 28, 34, 48, 50, 51] preserve the overall design while proposing algorithmic and structural refinements to tackle several limitations. In this work, we concentrate on Gaussian Shading style watermarking and primarily compare against the representative baseline Gaussian Shading [49].

3. Methods

In Sec. 3.1, we review the baseline, Gaussian Shading [49]. In Sec. 3.2, we introduce our One-step Inversion (OSI), a learning-based method that significantly improves the extraction of Gaussian Shading style watermarks. In Sec. 3.3, we describe the construction of our training data.

3.1. Preliminary: Gaussian Shading (GS)

Fig. 1(a) and Fig. 1(c) illustrate the Gaussian Shading (GS) watermarking system, which consists of three steps: 1) watermark encryption, 2) diffusion generation, and 3) watermark extraction.

Watermark Encryption GS employs repetition coding and XOR/ChaCha20 [3] to embed the watermark information into a sign mask. Specifically, the binary watermark $wm \in \{0, 1\}^{c \times \frac{h}{f_{hw}} \times \frac{w}{f_{hw}}}$ is first replicated along the height and width dimensions to match the latent shape $c \times h \times w$ of the diffusion model, where f_{hw} is the repetition factor for both height and width. Then, the repeated watermark is encrypted using XOR or ChaCha20 [3] to generate sign mask $m \in \{-1, +1\}^{c \times h \times w}$.

Diffusion Generation with GS Watermarks Given the sign mask m , the diffusion generation process with GS style watermark is formulated as follows,

$$I = \text{Dec}(f_{0 \leftarrow 1} \circ f_{1 \leftarrow 2} \circ \dots \circ f_{T-1 \leftarrow T}(\text{abs}(\tilde{z}) \odot m)), \quad (1)$$

where $f_{s \leftarrow t}$ denotes the latent diffusion model [40], Dec denotes the VAE decoder, and $\tilde{z} \sim \mathcal{N}(\mathbf{0}, \mathbf{I})$ denotes a Gaussian noise. As illustrated by $\text{abs}(\tilde{z}) \odot m$ in Eq. (1), GS conceals the watermark information as the signs of the initial noise.

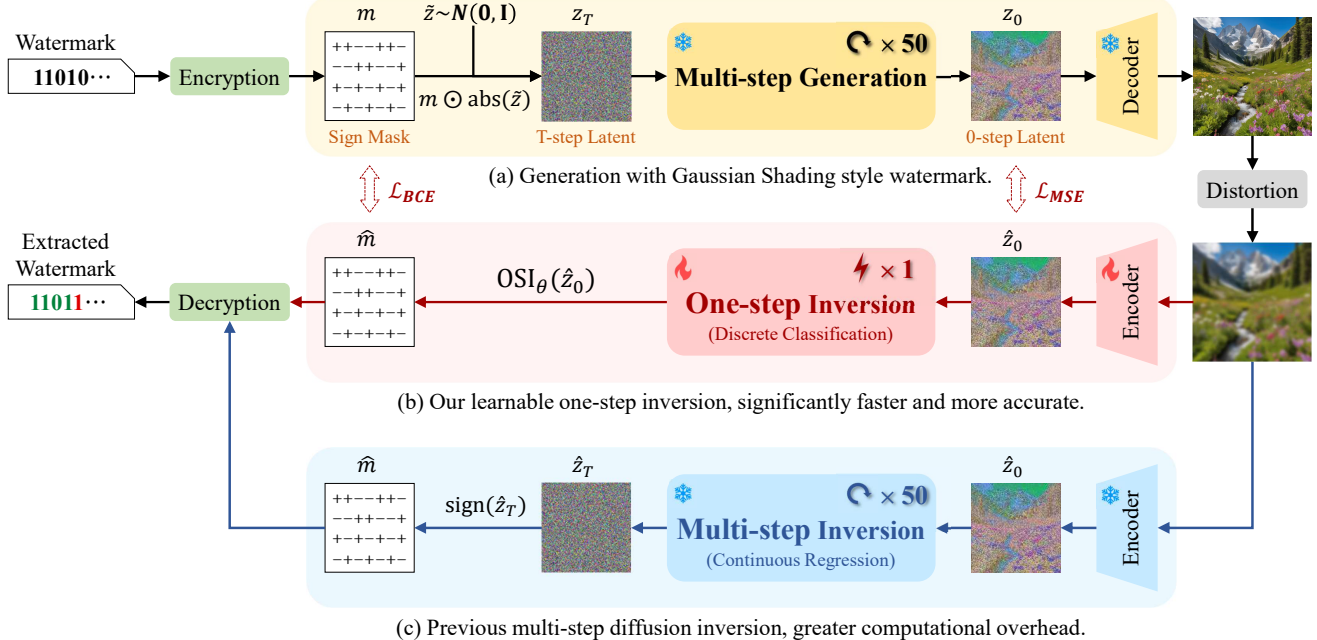


Figure 1. Overview of the proposed OSI method. For generation, (a) we embed Gaussian Shading style watermark, concealing watermark in the signs of initial latent. For extraction, (b) we adopt learnable one-step inversion (OSI) to directly predict the sign mask, while (c) previous methods first perform multi-step diffusion inversion to reconstruct continuous latent \hat{z}_T and then extract the sign of \hat{z}_T .

Multi-step Inversion for Watermark Extraction As can be seen from Eq. (1), the core problem of watermark extraction is to recover the signs m of the initial noise. To this end, GS first employs multi-step diffusion inversion [43] to recover the precise initial noise and then extracts the signs of the recovered noise, formulated as follows,

$$\hat{m} = \underline{\text{sign}}(f_{T \leftarrow T-1} \circ f_{T-1 \leftarrow T-2} \circ \dots \circ f_{1 \leftarrow 0}(\text{Enc}(I))), \quad (2)$$

where the inversion step T is typically set as 50. As a consequence, the watermark extraction requires 50 forward passes of the network $f_{t \leftarrow s}$, which is computationally expensive and time-consuming.

3.2. One-step Inversion for Watermark Extraction

Refocusing on the watermark extraction task itself, what we ultimately care about is the signs of the initial noise, rather than its precise value. What if we directly predict the signs, skipping the cumbersome inversion for exact initial noise? To this end, we propose One-step Inversion (OSI) for efficient extraction of GS style watermarks. As shown in Fig. 1(b), our OSI learns a sign classification model that predicts the signs directly in a single forward pass, formulated as follows,

$$\hat{m} = \text{sign}(p - 0.5), \quad p = \text{OSI}_\theta(\text{Enc}_\psi(I)), \quad (3)$$

where Enc_ψ is a trainable encoder that maps the watermarked image back to the latent space, OSI_θ is a trainable

sign classification model, and p denotes the predicted probability of the positive sign.

To optimize the model parameters, we employ binary cross-entropy loss for sign classification, as follows,

$$\mathcal{L}_{\text{BCE}} = -y \log(p) - (1 - y) \log(1 - p), \quad (4)$$

where $y = (m + 1)/2$ denotes the ground-truth label. In addition, we employ MSE loss between the encoded latent $\hat{z}_0 = \text{Enc}_\psi(I)$ and the original latent z_0 (see Fig. 1(a)), enforcing the latent-consistency to further improve the performance, as follows,

$$\mathcal{L}_{\text{MSE}} = \|\hat{z}_0 - z_0\|_2^2. \quad (5)$$

Overall, we train our OSI model with the objective:

$$\min_{\theta, \psi} \mathcal{L}_{\text{BCE}} + \mathcal{L}_{\text{MSE}}. \quad (6)$$

Besides, we initialize OSI_θ with the pretrained latent diffusion backbone and initialize Enc_ψ with the pretrained VAE encoder to leverage their inherent capability of exact noise inversion [43, 49], which we found to significantly benefit the training convergence. We also introduce data augmentation, e.g., resizing, blurring, and cropping, to the input images during training, which enhances the model's robustness to various distortions.

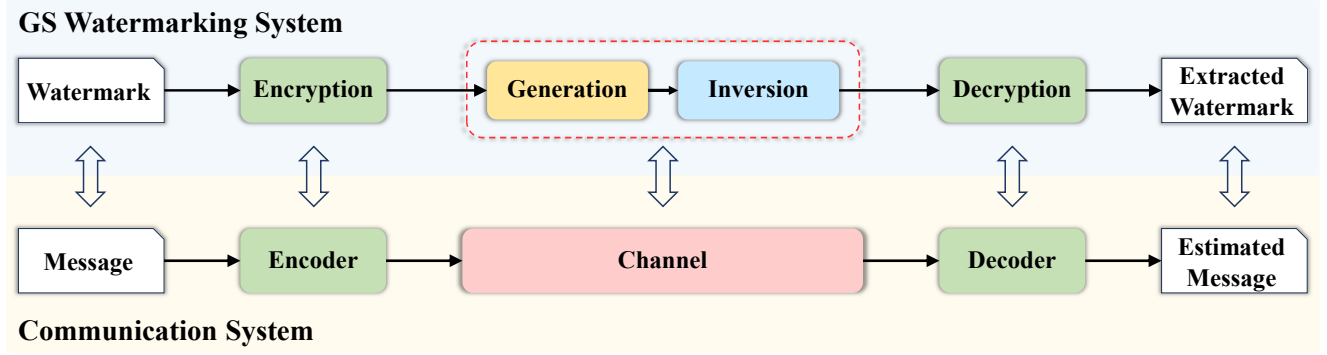


Figure 2. A communication system perspective on Gaussian Shading watermarking systems.

3.3. Training Data Construction

To train our OSI model, we construct a supervised dataset where each sample is a triplet (I, z_0, z_T) . Specifically, we 1) sample an initial noise $z_T \sim \mathcal{N}(\mathbf{0}, \mathbf{I})$ whose signs serve as the ground-truth m , 2) run the diffusion generation pipeline to obtain the 0-step latent z_0 that is used to calculate \mathcal{L}_{MSE} in Eq. (5), and 3) decode z_0 to obtain the synthesized image I that serves as the model input.

4. Communication System Perspective

In this section, we reinterpret the GS style watermarking from the perspective of **communication system**. As illustrated in Fig. 2, the watermark can be viewed as the message, the encryption and decryption modules can be viewed as the encoder and the decoder, and the generation-inversion process corresponds to a channel. From this perspective, we can decouple the watermarking system into two essential components: 1) the **channel** that transmits the watermark information and 2) the **coding** scheme that determines the way to encode and decode the watermarks.

According to Shannon’s theorem [42], every channel has an inherent channel capacity C , which serves as the theoretical upper bound for the reliable information rate R , i.e., $R < C$. Moreover, there exists a coding scheme such that R can approach C arbitrarily closely, and the error probability can be made arbitrarily small. Therefore, this principle implies two avenues for optimizing a watermarking system: 1) improving the coding methodology to enhance the information reliability and maximize the information rate R toward the channel capacity C , and 2) improving the channel itself to increase the channel capacity. From this perspective, we can classify existing GS style watermarking methods, including ours, into the following two categories.

Prior Works: Coding Improvement Most existing GS style approaches can be regarded as improving the coding scheme over a fixed channel, as they focus on the encryp-

tion module while maintaining the generation and inversion procedures unchanged. For example, GS [49] uses repetition codes (REP), PRCW [15] uses pseudo-random codes (PRC) [8], and GS++ [51] combines REP and PRC. Although these coding-centric approaches have made substantial advancements in enhancing both watermark reliability and payload capacity, their performance remains fundamentally constrained by the fixed channel capacity.

Our Work: Channel Improvement From the perspective of communication system, our approach can be viewed as an improvement of the channel. By explicitly training the inversion model to achieve higher bit accuracy, we effectively increase the channel capacity C , thereby improving the overall reliability of watermark extraction, as demonstrated in Sec. 5.2 and Sec. 5.4. Notably, several prior coding-centric studies [49, 51] have highlighted the need for more accurate diffusion inversion techniques [20, 21, 46] to enhance watermark extraction. From the perspective of communication system, the pursuit of these advanced diffusion inversion techniques can be interpreted as striving for more robust and efficient channels.

Based on the preceding analysis, we have demonstrated a clear connection between the GS watermarking system and the communication system. The latter has evolved over many years and is characterized by robust theories and advanced techniques. In this light, certain research challenges within the GS watermarking system may be reformulated in terms of communication system paradigms, thereby enabling the adoption of mature theories and techniques from communication system. We hope that this communication system perspective will offer broader and novel insights into the GS watermarking system and promote further advancements in future research.

Table 1. Evaluation results on SD2.1. ‘‘Adv.’’ denotes the average performance in all adversarial scenarios. Across all f_{hw} settings, OSI outperforms GS [49] in TPR, bit accuracy, and payload rate, while substantially reducing FLOPs by over $20\times$ and achieving $25\times$ speedup.

Method	f_{hw}	TPR@FPR=1e-6		Bit Accuracy		Payload Rate	FLOPs (T)	A100 Time (s)
		Clean	Adv.	Clean	Adv.			
GS	1	1.0000	0.9982	0.8560	0.6616	7.67%	41.3	1.52
	2	1.0000	0.9967	0.9408	0.7298	3.96%		
	4	1.0000	0.9964	0.9984	0.8784	2.91%		
	8	1.0000	0.9970	1.0000	0.9728	1.28%		
OSI (ours)	1	1.0000	0.9991	0.8839	0.7364	16.8%	1.92	0.06
	2	1.0000	0.9984	0.9607	0.8189	7.94%		
	4	1.0000	0.9986	0.9996	0.9491	4.44%		
	8	1.0000	0.9984	1.0000	0.9939	1.48%		

5. Experiment

In Sec. 5.1, we introduce implementation details. In Sec. 5.2, we present experimental results of OSI on SD2.1, which shows superiority in both performance and efficiency. In Sec. 5.3, we provide detailed ablation studies. In Sec. 5.4, we demonstrate the broad generality of OSI across diffusion models, schedulers, and cryptographic schemes.

5.1. Implementation detail

Diffusion Models We focus on text-to-image latent diffusion models and select Stable Diffusion (SD) [40] to conduct experiments. The majority of experiments run with SD2.1 [40] to align with GS [49], producing 512×512 images from $4 \times 64 \times 64$ latents. To assess generality, we also conduct experiments on SDXL [38] for higher resolution (1024×1024 images and $4 \times 128 \times 128$ latents), and SD3.5 [10] for flow matching [30, 31] mechanism and DiT [37] backbone (1024×1024 images and $16 \times 128 \times 128$ latents). For all SD variants we adopt classifier-free guidance (CFG) [19], using a guidance scale of 7.5 during generation and disabling it during inversion (scale set to 1).

Schedulers Following GS [49], for SD2.1 and SDXL, we sample with 50-step DPM-Solver [32] and inverse with 50-step DDIM scheduler [43]. For SD3.5, we use the default Euler–discrete scheduler [10] with 28 steps of sampling and inversion. Note that the inversion schedulers apply only to the baselines. Our OSI inverses one step without scheduler.

Dataset We use the Stable Diffusion Prompts (SDP) corpus [16]. Following GS [49], the first 1k prompts are reserved for evaluation, while the remaining $\sim 72k$ prompts are used to synthesize the noise–image pairs described in Sec. 3.3. To assess cross-dataset generality, we additionally evaluate on prompts from MS-COCO [29].

Finetuning Setting We finetune the OSI model for 11 epochs with a batch size of 16 using Adam [25] and a learning rate of 1×10^{-4} . Random data augmentation (cropping, blurring, etc.) is applied with probability 50%.

Evaluation Metrics Following GS [49], we report 1) the true positive rate at a fixed false positive rate of 10^{-6} (TPR@FPR=1e-6; detailed in the Appendix) and 2) bit accuracy of the recovered watermark. To assess robustness, we also adopt the nine representative adversarial distortions used in GS [49] (see Appendix). To quantify efficiency, we measure FLOPs and the payload rate (see Sec. 5.2). Note that we only modify the extraction pipeline relative to prior methods [15, 48, 49]. Therefore, image quality metrics (e.g., FID [18] and CLIP-Score [39]) are expected to be essentially identical and thus are not considered in our study.

5.2. Performance of One-step inversion (OSI)

Performance Gain In Tab. 1, we compare our OSI with the GS [49] baseline under four different f_{hw} settings on SD2.1. Generally, larger f_{hw} values yield higher bit accuracy but correspond to shorter embedded watermarks. Across all f_{hw} configurations, OSI consistently outperforms GS, achieving higher bit accuracy and TPR in both clean and adversarial scenarios. The cross-dataset evaluations on MS-COCO [29] exhibit the same performance trends, as shown in Tab. 2, indicating that the advantages of OSI are not tied to a specific training distribution and transfer robustly to a different domain.

Computational Efficiency As shown in Tab. 1, OSI reduces the computational cost by more than $20\times$ in terms of FLOPs. To further quantify the practical benefit, we also measure the per-extraction wall-clock time on a single NVIDIA A100 40G GPU. The results in Tab. 1 corroborate the efficiency gain, showing more than $25\times$ speedup in runtime, which confirms that OSI delivers substantial gains in both computation and actual inference latency.

Table 2. Comparison with GS [49] on MS-COCO [29] dataset.

Method	f_{hw}	Clean	Adv.	Payload Rate
GS	1	0.8652	0.6616	7.67%
	2	0.9473	0.7290	3.93%
	4	0.9992	0.8760	2.87%
	8	1.0000	0.9697	1.26%
OSI (ours)	1	0.8815	0.7326	16.2%
	2	0.9590	0.8134	7.64%
	4	0.9997	0.9445	4.32%
	8	1.0000	0.9931	1.47%

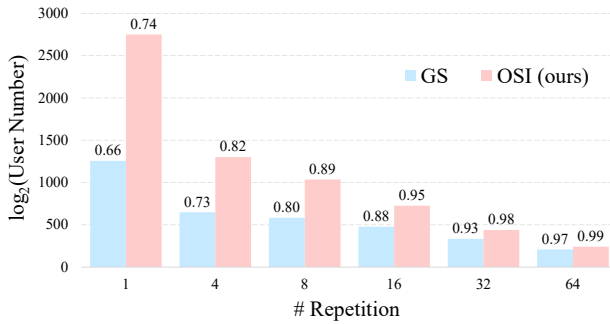


Figure 3. Comparison of user number across repetition count settings. Numbers above the bars display the corresponding bit accuracies. The higher accuracy of OSI yields an exponentially larger addressable user number than GS [49].

Amortized Training Cost at Scale Although the improvements of OSI are obtained at the expense of finetuning, this cost is negligible when amortized over downstream deployment at scale. The finetuning procedure described in Sec. 5.1 requires only about 15 hours on 8 NVIDIA A100 40G GPUs, corresponding to roughly $1.92T \times 11 \times 72k \approx 1.52E$ FLOPs in total. Given that OSI saves about 39T FLOPs per extraction run, only $1.52E \div 39T \approx 39k$ extraction runs are needed to fully amortize the finetuning compute, which is well within the scale of platform-level deployments. Moreover, as shown in Sec. 5.4, the finetuned OSI model generalizes across diverse generation schedulers and cryptographic schemes, allowing a single finetuning investment to support a broad range of scenarios. Overall, this one-time finetuning expense yields a highly favorable return on compute and is amortized rapidly at scale.

Payload Rate From a communication-theoretic perspective, we analyze the payload rate R of GS and OSI, which quantifies the amount of effective watermark information that can be embedded per position in z_T . We model the watermarking-extraction procedure as a binary symmetric channel (BSC) with crossover probability $p = 1 - a$, where a is the bit accuracy reported in Tab. 1. According to Shan-

Table 3. Performance under advanced attacks.

		f_{hw}			
		1	2	4	8
Compression	GS	0.6253	0.6822	0.8264	0.9460
	OSI	0.6339	0.6941	0.8434	0.9584
Embedding	GS	0.6394	0.7003	0.8585	0.9647
	OSI	0.6483	0.7188	0.8804	0.9758

non’s theorem [42], the channel capacity of this BSC is

$$C_{\text{BSC}} = 1 - H(p) = 1 + p \log_2 p + (1 - p) \log_2(1 - p), \quad (7)$$

which characterizes the maximum proportion of effective payload bits in communication. Considering the f_{hw}^2 replication used in GS, the payload rate R is calculated as

$$R = \frac{C_{\text{BSC}}}{f_{hw}^2}. \quad (8)$$

Thus, when using an error-correcting code (ECC) that operates close to the capacity C_{BSC} , the maximum reliably embedded payload in the latent z_T is $R \times c \times h \times w$ bits. Notably, when $f_{hw} = 1$, OSI avoids replication (no coding involved) and achieves a $2 \times$ higher payload rate than GS, indicating OSI can consistently outperform GS under the same coding scheme.

For an intuitive comparison between OSI and GS, we use all effective payload bits to encode a user identifier, which allows for $2^{R \times c \times h \times w}$ distinct users in total. We visualize the resulting gap in the user number between OSI and GS in Fig. 3. By improving bit accuracies, OSI achieves higher payload rates $R_{\text{OSI}} > R_{\text{GS}}$, thereby supporting exponentially larger user numbers than GS.

Advanced Attack We introduce two types of advanced attacks to evaluate the performance of OSI under more rigorous conditions. The first type is compression attack, where pretrained VAEs [1, 7, 36] are used to encode and decode watermarked images to emulate realistic lossy compression in practical deployment. The second type is embedding attack [24], which generates perturbations that are nearly imperceptible in pixel space but significantly different in feature embedding space (ResNet/CLIP) [17, 39]. In this way, embedding attacks can induce extraction failures, particularly for watermarking methods that operate at the latent or feature level. As summarized in Tab. 3, OSI consistently outperforms GS under both attack types.

5.3. Ablation Study

OSI Model Design The default OSI model comprises the encoder and the diffusion backbone model (UNet of SD2.1)

Table 4. Module ablation on SD2.1. We compare different settings without data augmentation. Across all f_{hw} configurations, jointly finetuning the UNet and encoder achieves the best performance in both clean and adversarial scenarios.

Method	Clean				Adversarial			
	1	2	4	8	1	2	4	8
Baseline (GS)	0.8560	0.9408	0.9984	1.0000	0.6616	0.7298	0.8784	0.9728
Frozen	0.7241	0.8119	0.9612	0.9985	0.6148	0.6682	0.8041	0.9316
Tune UNet	0.8810	0.9507	0.9991	1.0000	0.6664	0.7342	0.8831	0.9749
Tune UNet & Encoder (OSI)	0.8865	0.9625	0.9997	1.0000	0.6729	0.7445	0.8953	0.9809

of the generation pipeline, leveraging their watermark extraction capability demonstrated in multi-step diffusion inversion [15, 49]. A natural question is whether these components can be directly utilized for one-step inversion. We first evaluate a fully frozen configuration, fixing the encoder and the U-Net and performing one-step extraction. The “Frozen” result in Tab. 4 shows certain one-step inversion capability, but performance lags markedly behind the GS baseline, indicating that finetuning is necessary. We then consider two fine-tuning settings: 1) freezing the encoder and finetuning only the U-Net; and 2) finetuning both the encoder and the U-Net. Both settings outperform the GS baseline, with the best results obtained when finetuning both modules. Accordingly, we adopt joint finetuning as the default configuration.

Conceptually, we formulate the watermark extraction as a classification problem, any sufficiently capable classifier could be used. Why not train a lightweight model from scratch? In practice, finetuning the pretrained diffusion modules is more reliable: it leverages features already aligned with the latent space, stabilizes optimization, and avoids the overhead of crafting new architectures and training schedules. As a reference point, we randomly initialize a U-Net and train it under identical settings. As shown in Fig. 4, the training of random initialization collapses and fails to converge. Collectively, these analyses and observations confirm that the initialization with the parameters of the encoder and diffusion backbone model is a sensible and effective choice for our OSI model.

Data Augmentation With probability 0.5, we apply a random type of image distortion to the inputs during finetuning to improve the robustness of OSI. The data augmentation is not tailored to the evaluation protocol. Instead, it helps OSI tolerate a broader range of image distortions. As shown in Tab. 5, with $f_{hw} = 1$, finetuning without data augmentation already exceeds GS baseline, while adding augmentation further boost performances in adversarial scenarios, with only a minor drop in the clean scenario.

Classifier-Free Guidance (CFG) We set the CFG scale to 7.5 when synthesizing our dataset for finetuning the OSI

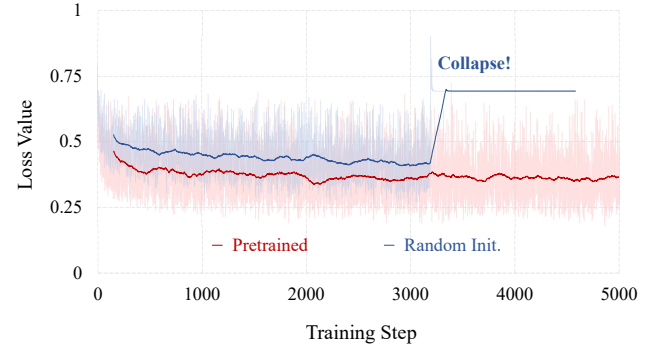


Figure 4. Training loss comparison between different initializations of UNet parameters. Random initialization encounters training collapse and fails to converge.

Table 5. Performance of OSI with and without data augmentation.

	GS	OSI w/o	OSI w/
Clean	0.8560	0.8865	0.8839
Adversarial	0.6616	0.6729	0.7364

Table 6. Performances across different CFG scales.

		CFG				
		1	3	5	7.5	10
Clean	GS	0.9263	0.9044	0.8826	0.8560	0.8307
	OSI	0.9362	0.9217	0.9057	0.8839	0.8604
Adversarial	GS	0.7281	0.7007	0.6801	0.6616	0.6474
	OSI	0.7963	0.7738	0.7553	0.7364	0.7199

model. Considering the variety of CFG scales applied during generation, we assess the performance of OSI under different guidance scales with $f_{hw} = 1$ in Tab. 6. OSI consistently outperforms GS across all tested CFG settings, despite being trained solely on noise–image pairs which are generated with CFG scale of 7.5.

5.4. Broader Application

SDXL We extend OSI to SDXL [38] to test performance in high-resolution generation. Analogous to SD 2.1, we

Table 7. Comparison with GS [49] on SDXL.

Method	f_{hw}	Clean	Adv.	Payload Rate	FLOPs(T)
GS	1	0.7845	0.6123	3.67%	303.3
	2	0.8789	0.6649	2.00%	
	4	0.9894	0.8008	1.75%	
	8	0.9999	0.9305	0.99%	
OSI (ours)	1	0.8276	0.6676	8.26%	10.3
	2	0.9185	0.7395	4.31%	
	4	0.9963	0.8914	3.15%	
	8	1.0000	0.9790	1.33%	

Table 8. Comparison with GS [49] on SD3.5.

Method	f_{hw}	Clean	Adv.	Payload Rate	FLOPs(T)
GS	1	0.7604	0.5810	1.90%	200.9
	2	0.8520	0.6197	1.04%	
	4	0.9746	0.7278	0.97%	
	8	0.9982	0.8572	0.64%	
OSI (ours)	1	0.7978	0.6347	5.30%	11.4
	2	0.8887	0.6935	2.77%	
	4	0.9858	0.8359	2.22%	
	8	0.9993	0.9551	1.15%	

Table 9. Comparison of different scheduler pairs on clean images.

Model	Generation Scheduler	Inversion Scheduler	Bit Acc.		FLOPs(T)	
			GS	OSI	GS	OSI
SD2.1	DDIM	DDIM	0.8537	0.8805	41.3	1.92
		DDIM	0.8560	0.8839	41.3	1.92
	DPM-Solver	DPM-Solver	0.8655	0.8839	197.8	1.92
SDXL	DDIM	DDIM	0.8524	0.8774	303.3	10.3
		DDIM	0.7845	0.8276	303.3	10.3
	DPM-Solver	DPM-Solver	0.6611	0.8276	1738	10.3

synthesize a noise–image dataset at corresponding shapes and finetune OSI using the default configuration in Sec. 5.3. As shown in Tab. 7, OSI mirrors the trends observed on SD2.1: it delivers higher accuracy and payload rate while requiring substantially fewer FLOPs.

SD3.5 We also extend OSI to SD3.5 [10], a model based on the flow matching [30, 31] mechanism and the DiT architecture [37]. We synthesize the dataset and fine-tune OSI as before. The results reported in Tab. 8 again demonstrate that OSI outperforms GS in performance and efficiency.

Scheduler We assess OSI using three (generation — inversion) scheduler configurations: (DPM-Solver [32] — DPM-Solver), (DPM-Solver — DDIM [43]), and (DDIM — DDIM). Notably, OSI only depends on the generation scheduler, whereas GS relies on both generation scheduler and inversion scheduler. The performance of the three com-

Table 10. Comparison with PRC [15] on SD2.1.

		Watermark Bits				
		4096	2048	1024	512	256
Clean	PRC	0.8751	0.9480	1.0000	1.0000	1.0000
	OSI	0.8752	0.9605	1.0000	1.0000	1.0000
Adversarial	PRC	0.8751	0.9376	0.9739	0.9903	0.9972
	OSI	0.8751	0.9395	0.9925	0.9993	0.9997

Table 11. Comparison with T2SMARK [48] on SD2.1.

		Watermark Bits				
		4096	2048	1024	512	256
Clean	T2S	0.9909	0.9979	0.9998	1.0000	1.0000
	OSI	0.9977	0.9998	1.0000	1.0000	1.0000
Adversarial	T2S	0.7993	0.8635	0.9387	0.9756	0.9909
	OSI	0.8943	0.9407	0.9884	0.9980	0.9991

bined scheduler settings in Tab. 9 ($f_{hw} = 1$) shows that OSI consistently outperforms GS across all settings with higher bit accuracy and significantly lower FLOPs.

PRCW Since OSI does not alter the cryptography operations, it can be applied to other GS style methods that adopt different codes. Here we apply OSI to PRCW [15], which leverages the PRC [8] code. We integrate OSI with PRCW [15] by replacing its multi-step diffusion inversion with the finetuned OSI model. As shown in Tab. 10, across all settings of watermark bits, OSI achieves higher bit accuracy.

T2SMARK We further evaluate OSI on T2SMARK [48], a recent method which follows the GS framework but introduces tail-truncated sampling in the cryptographic stage. After substituting the original multi-step inversion with the finetuned OSI model, we achieve higher bit accuracy across all settings in Tab. 11, confirming the superiority of OSI.

6. Conclusion

We revisit Gaussian Shading style watermarking from communication system perspective and reformulate watermark extraction as a discrete classification problem rather than a reduced form of continuous latent regression. Building on these views, we propose One-step Inversion (OSI), a learnable one-step watermark extractor that serves as a channel improvement to the GS framework. Extensive experiments across various schedulers, diffusion models, and cryptographic schemes demonstrate that OSI consistently offers stronger extraction performance, higher payload capacity, and substantially lower computational cost compared with existing approaches. We hope our work and perspective provide practical and principled references for developing more efficient and robust diffusion watermarking systems.

References

[1] Johannes Ballé, David Minnen, Saurabh Singh, Sung Jin Hwang, and Nick Johnston. Variational image compression with a scale hyperprior. In *6th International Conference on Learning Representations, ICLR 2018, Vancouver, BC, Canada, April 30 - May 3, 2018, Conference Track Proceedings*. OpenReview.net, 2018. [6](#) [4](#)

[2] Mauro Barni, Franco Bartolini, Vito Cappellini, and Alessandro Piva. A dct-domain system for robust image watermarking. *Signal Process.*, 66(3):357–372, 1998. [1](#)

[3] Daniel J. Bernstein. Chacha, a variant of salsa20. Technical report, 2008. [2](#) [5](#)

[4] Andrew P. Bradley. The use of the area under the ROC curve in the evaluation of machine learning algorithms. *Pattern Recognit.*, 30(7):1145–1159, 1997. [1](#)

[5] Brian Chen and Gregory W. Wornell. Quantization index modulation: A class of provably good methods for digital watermarking and information embedding. *IEEE Trans. Inf. Theory*, 47(4):1423–1443, 2001. [1](#)

[6] Yuzhuo Chen, Zehua Ma, Han Fang, Weiming Zhang, and Nenghai Yu. Tag-wm: Tamper-aware generative image watermarking via diffusion inversion sensitivity. In *Proceedings of the IEEE/CVF International Conference on Computer Vision (ICCV)*, pages 16723–16732, 2025. [1](#) [2](#)

[7] Zhengxue Cheng, Heming Sun, Masaru Takeuchi, and Jiro Katto. Learned image compression with discretized gaussian mixture likelihoods and attention modules. In *2020 IEEE/CVF Conference on Computer Vision and Pattern Recognition, CVPR 2020, Seattle, WA, USA, June 13-19, 2020*, pages 7936–7945. Computer Vision Foundation / IEEE, 2020. [6](#) [4](#)

[8] Miranda Christ and Sam Gunn. Pseudorandom error-correcting codes. *IACR Cryptol. ePrint Arch.*, page 235, 2024. [2](#) [4](#) [8](#)

[9] Hai Ci, Pei Yang, Yiren Song, and Mike Zheng Shou. Ringid: Rethinking tree-ring watermarking for enhanced multi-key identification. In *Computer Vision - ECCV 2024 - 18th European Conference, Milan, Italy, September 29-October 4, 2024, Proceedings, Part XXVIII*, pages 338–354. Springer, 2024. [1](#) [2](#)

[10] Patrick Esser, Sumith Kulal, Andreas Blattmann, Rahim Entezari, Jonas Müller, Harry Saini, Yam Levi, Dominik Lorenz, Axel Sauer, Frederic Boesel, Dustin Podell, Tim Dockhorn, Zion English, and Robin Rombach. Scaling rectified flow transformers for high-resolution image synthesis. In *Forty-first International Conference on Machine Learning, ICML 2024, Vienna, Austria, July 21-27, 2024*. OpenReview.net, 2024. [5](#) [8](#)

[11] Weitao Feng, Wenbo Zhou, Jiyan He, Jie Zhang, Tianyi Wei, Guanlin Li, Tianwei Zhang, Weiming Zhang, and Nenghai Yu. Aqualora: Toward white-box protection for customized stable diffusion models via watermark lora. In *Forty-first International Conference on Machine Learning, ICML 2024, Vienna, Austria, July 21-27, 2024*. OpenReview.net, 2024. [2](#)

[12] Pierre Fernandez, Guillaume Couairon, Hervé Jégou, Matthijs Douze, and Teddy Furon. The stable signature: Rooting watermarks in latent diffusion models. In *IEEE/CVF International Conference on Computer Vision, ICCV 2023, Paris, France, October 1-6, 2023*, pages 22409–22420. IEEE, 2023. [2](#)

[13] Kevin Frans, Danijar Hafner, Sergey Levine, and Pieter Abbeel. One step diffusion via shortcut models. In *The Thirteenth International Conference on Learning Representations, ICLR 2025, Singapore, April 24-28, 2025*. OpenReview.net, 2025. [1](#)

[14] Zhengyang Geng, Mingyang Deng, Xingjian Bai, J. Zico Kolter, and Kaiming He. Mean flows for one-step generative modeling, 2025. [1](#)

[15] Sam Gunn, Xuandong Zhao, and Dawn Song. An undetectable watermark for generative image models. In *The Thirteenth International Conference on Learning Representations, ICLR 2025, Singapore, April 24-28, 2025*. OpenReview.net, 2025. [1](#) [2](#) [4](#) [5](#) [7](#) [8](#) [3](#)

[16] Gustavosta. Stable-diffusion-prompts. <https://huggingface.co/datasets/Gustavosta/Stable-Diffusion-Prompts>, 2024. Accessed: 2025-11-01. [5](#)

[17] Kaiming He, Xiangyu Zhang, Shaoqing Ren, and Jian Sun. Deep residual learning for image recognition. In *2016 IEEE Conference on Computer Vision and Pattern Recognition, CVPR 2016, Las Vegas, NV, USA, June 27-30, 2016*, pages 770–778. IEEE Computer Society, 2016. [6](#) [5](#)

[18] Martin Heusel, Hubert Ramsauer, Thomas Unterthiner, Bernhard Nessler, and Sepp Hochreiter. Gans trained by a two time-scale update rule converge to a local nash equilibrium. In *Advances in Neural Information Processing Systems 30: Annual Conference on Neural Information Processing Systems 2017, December 4-9, 2017, Long Beach, CA, USA*, pages 6626–6637, 2017. [5](#)

[19] Jonathan Ho and Tim Salimans. Classifier-free diffusion guidance. *CoRR*, abs/2207.12598, 2022. [5](#)

[20] Seongmin Hong, Suh Yoon Jeon, Kyeonghyun Lee, Ernest K. Ryu, and Se Young Chun. Gradient-free decoder inversion in latent diffusion models. In *Advances in Neural Information Processing Systems 38: Annual Conference on Neural Information Processing Systems 2024, NeurIPS 2024, Vancouver, BC, Canada, December 10 - 15, 2024*, 2024. [4](#)

[21] Seongmin Hong, Kyeonghyun Lee, Suh Yoon Jeon, Hyewon Bae, and Se Young Chun. On exact inversion of dpm-solvers. In *IEEE/CVF Conference on Computer Vision and Pattern Recognition, CVPR 2024, Seattle, WA, USA, June 16-22, 2024*, pages 7069–7078. IEEE, 2024. [4](#)

[22] Edward J. Hu, Yelong Shen, Phillip Wallis, Zeyuan Allen-Zhu, Yuanzhi Li, Shean Wang, Lu Wang, and Weizhu Chen. Lora: Low-rank adaptation of large language models. In *The Tenth International Conference on Learning Representations, ICLR 2022, Virtual Event, April 25-29, 2022*. OpenReview.net, 2022. [2](#)

[23] Huayang Huang, Yu Wu, and Qian Wang. ROBIN: robust and invisible watermarks for diffusion models with adversarial optimization. In *Advances in Neural Information Processing Systems 38: Annual Conference on Neural Information Processing Systems 2024, NeurIPS 2024, Vancouver, BC, Canada, December 10 - 15, 2024*, 2024. [2](#)

[24] Nathan Inkawich, Wei Wen, Hai (Helen) Li, and Yiran Chen. Feature space perturbations yield more transferable adversarial examples. In *IEEE Conference on Computer Vision and Pattern Recognition, CVPR 2019, Long Beach, CA, USA, June 16-20, 2019*, pages 7066–7074. Computer Vision Foundation / IEEE, 2019. 6

[25] Diederik P. Kingma and Jimmy Ba. Adam: A method for stochastic optimization. In *3rd International Conference on Learning Representations, ICLR 2015, San Diego, CA, USA, May 7-9, 2015, Conference Track Proceedings*, 2015. 5

[26] Sung Ju Lee and Nam Ik Cho. Semantic watermarking reinvented: Enhancing robustness and generation quality with fourier integrity. In *Proceedings of the IEEE/CVF International Conference on Computer Vision*, pages 18759–18769, 2025. 1, 2

[27] Liangqi Lei, Keke Gai, Jing Yu, Liehuang Zhu, and Qi Wu. Secure and efficient watermarking for latent diffusion models in model distribution scenarios. In *Proceedings of the Thirty-Fourth International Joint Conference on Artificial Intelligence, IJCAI 2025, Montreal, Canada, August 16-22, 2025*, pages 7473–7481. ijcai.org, 2025. 2

[28] Kecen Li, Zhicong Huang, Xinwen Hou, and Cheng Hong. Gaussmarker: Robust dual-domain watermark for diffusion models. In *Proceedings of the 42nd International Conference on Machine Learning*, pages 34688–34701. PMLR, 2025. 1, 2

[29] Tsung-Yi Lin, Michael Maire, Serge J. Belongie, James Hays, Pietro Perona, Deva Ramanan, Piotr Dollár, and C. Lawrence Zitnick. Microsoft COCO: common objects in context. In *Computer Vision - ECCV 2014 - 13th European Conference, Zurich, Switzerland, September 6-12, 2014, Proceedings, Part V*, pages 740–755. Springer, 2014. 5, 6

[30] Yaron Lipman, Ricky T. Q. Chen, Heli Ben-Hamu, Maximilian Nickel, and Matthew Le. Flow matching for generative modeling. In *The Eleventh International Conference on Learning Representations, ICLR 2023, Kigali, Rwanda, May 1-5, 2023*. OpenReview.net, 2023. 5, 8

[31] Xingchao Liu, Chengyue Gong, and Qiang Liu. Flow straight and fast: Learning to generate and transfer data with rectified flow. In *The Eleventh International Conference on Learning Representations, ICLR 2023, Kigali, Rwanda, May 1-5, 2023*. OpenReview.net, 2023. 5, 8

[32] Cheng Lu, Yuhao Zhou, Fan Bao, Jianfei Chen, Chongxuan Li, and Jun Zhu. Dpm-solver: A fast ODE solver for diffusion probabilistic model sampling in around 10 steps. In *Advances in Neural Information Processing Systems 35: Annual Conference on Neural Information Processing Systems 2022, NeurIPS 2022, New Orleans, LA, USA, November 28 - December 9, 2022*. 5, 8

[33] Weijian Luo, Zemin Huang, Zhengyang Geng, J. Zico Kolter, and Guo-Jun Qi. One-step diffusion distillation through score implicit matching. In *Advances in Neural Information Processing Systems 38: Annual Conference on Neural Information Processing Systems 2024, NeurIPS 2024, Vancouver, BC, Canada, December 10 - 15, 2024*, 2024. 1

[34] Po-Yuan Mao, Cheng-Chang Tsai, and Chun-Shien Lu. Maxsive: High-capacity and robust training-free generative image watermarking in diffusion models. In *Proceedings of the 33rd ACM International Conference on Multimedia, New York, NY, USA, 2025*. Association for Computing Machinery. 1, 2

[35] Inc. Midjourney. Midjourney: Ai image generation platform. <https://www.midjourney.com/>, 2025. Accessed: Nov. 5, 2025. 1

[36] David Minnen, Johannes Ballé, and George Toderici. Joint autoregressive and hierarchical priors for learned image compression. In *Advances in Neural Information Processing Systems 31: Annual Conference on Neural Information Processing Systems 2018, NeurIPS 2018, December 3-8, 2018, Montréal, Canada*, pages 10794–10803, 2018. 6, 4

[37] William Peebles and Saining Xie. Scalable diffusion models with transformers. In *IEEE/CVF International Conference on Computer Vision, ICCV 2023, Paris, France, October 1-6, 2023*, pages 4172–4182. IEEE, 2023. 5, 8

[38] Dustin Podell, Zion English, Kyle Lacey, Andreas Blattmann, Tim Dockhorn, Jonas Müller, Joe Penna, and Robin Rombach. SDXL: improving latent diffusion models for high-resolution image synthesis. In *The Twelfth International Conference on Learning Representations, ICLR 2024, Vienna, Austria, May 7-11, 2024*. OpenReview.net, 2024. 5, 7

[39] Alec Radford, Jong Wook Kim, Chris Hallacy, Aditya Ramesh, Gabriel Goh, Sandhini Agarwal, Girish Sastry, Amanda Askell, Pamela Mishkin, Jack Clark, Gretchen Krueger, and Ilya Sutskever. Learning transferable visual models from natural language supervision. In *Proceedings of the 38th International Conference on Machine Learning, ICML 2021, 18-24 July 2021, Virtual Event*, pages 8748–8763. PMLR, 2021. 5, 6

[40] Robin Rombach, Andreas Blattmann, Dominik Lorenz, Patrick Esser, and Björn Ommer. High-resolution image synthesis with latent diffusion models. In *IEEE/CVF Conference on Computer Vision and Pattern Recognition, CVPR 2022, New Orleans, LA, USA, June 18-24, 2022*, pages 10674–10685. IEEE, 2022. 2, 5

[41] Inc. Runway AI. Runway: Ai image and video generator. <https://runwayml.com/>, 2025. Accessed: Nov. 5, 2025. 1

[42] Claude E. Shannon. A mathematical theory of communication. *Bell System Technical Journal*, 27(3):379–423, 1948. Part II: 27(4): 623–656. 4, 6

[43] Jiaming Song, Chenlin Meng, and Stefano Ermon. Denoising diffusion implicit models. In *9th International Conference on Learning Representations, ICLR 2021, Virtual Event, Austria, May 3-7, 2021*. OpenReview.net, 2021. 2, 3, 5, 8

[44] Kuaishou Technology. Kling ai: Ai image and video generation platform. <https://klingai.com>, 2025. Accessed: Nov. 5, 2025. 1

[45] Ron G. van Schyndel, Andrew Z. Tirkel, and Charles F. Osborne. A digital watermark. In *Proceedings 1994 International Conference on Image Processing, Austin*,

Texas, USA, November 13-16, 1994, pages 86–90. IEEE Computer Society, 1994. [1](#)

[46] Bram Wallace, Akash Gokul, and Nikhil Naik. EDICT: exact diffusion inversion via coupled transformations. In IEEE/CVF Conference on Computer Vision and Pattern Recognition, CVPR 2023, Vancouver, BC, Canada, June 17-24, 2023, pages 22532–22541. IEEE, 2023. [4](#)

[47] Yuxin Wen, John Kirchenbauer, Jonas Geiping, and Tom Goldstein. Tree-rings watermarks: Invisible fingerprints for diffusion images. In Advances in Neural Information Processing Systems 36: Annual Conference on Neural Information Processing Systems 2023, NeurIPS 2023, New Orleans, LA, USA, December 10 - 16, 2023, 2023. [1, 2](#)

[48] Jindong Yang, Han Fang, Weiming Zhang, Nenghai Yu, and Kejiang Chen. T2smark: Balancing robustness and diversity in noise-as-watermark for diffusion models, 2025. [1, 2, 5, 8, 3, 4](#)

[49] Zijin Yang, Kai Zeng, Kejiang Chen, Han Fang, Weiming Zhang, and Nenghai Yu. Gaussian shading: Provably performance-lossless image watermarking for diffusion models. In IEEE/CVF Conference on Computer Vision and Pattern Recognition, CVPR 2024, Seattle, WA, USA, June 16-22, 2024, pages 12162–12171. IEEE, 2024. [1, 2, 3, 4, 5, 6, 7, 8](#)

[50] Zhonghao Yang, Linye Lyu, Xuanhang Chang, Daojing He, and YU LI. SWA-LDM: Toward stealthy watermarks for latent diffusion models. In The 1st Workshop on GenAI Watermarking, 2025. [1, 2](#)

[51] Zijin Yang, Xin Zhang, Kejiang Chen, Kai Zeng, Qiyi Yao, Han Fang, Weiming Zhang, and Nenghai Yu. Gaussian shading++: Rethinking the realistic deployment challenge of performance-lossless image watermark for diffusion models, 2025. [2, 4](#)

[52] Lijun Zhang, Xiao Liu, Antoni Viros Martin, Cindy Xiong Bearfield, Yuriy Brun, and Hui Guan. Attack-resilient image watermarking using stable diffusion. In Advances in Neural Information Processing Systems 38: Annual Conference on Neural Information Processing Systems 2024, NeurIPS 2024, Vancouver, BC, Canada, December 10 - 15, 2024, 2024. [1, 2](#)

[53] Yunqing Zhao, Tianyu Pang, Chao Du, Xiao Yang, Ngai-Man Cheung, and Min Lin. A recipe for watermarking diffusion models. CoRR, abs/2303.10137, 2023. [2](#)

OSI: One-step Inversion Excels in Extracting Diffusion Watermarks

Supplementary Material

A. Application Scenario

We consider the application scenario which involves a service provider, users and infringers. The service provider deploys a diffusion generation model on the platform but does not release the source codes or model weights. Users access the diffusion model via an API to generate images, which they may subsequently publish or distribute for their own purposes. Infringers may then appropriate these generated images and falsely claim copyright ownership over them. In this scenario, the service provider embeds a watermark at generation time to address two safety objectives: **detection** and **traceability**.

For detection, the service provider embeds a watermark that serves as a provenance marker, indicating that an image was generated by the provider's model and deterring misappropriation by infringers.

For traceability, the provider records user-specific identity metadata into the watermark to protect the rights of legitimate users, support dispute resolution, and enable accountable tracing of abusive behavior (e.g., generating malicious or harmful content).

B. Evaluation Metrics

B.1. Bit Accuracy

For each watermarked image, we define the bit accuracy as the proportion of matched bits between the embedded k -bit watermark $wm \in \{0, 1\}^k$ and the extracted watermark \hat{wm} :

$$Acc(wm, \hat{wm}) = \frac{1}{k} \sum_{i=1}^k \mathbf{1}(wm_i = \hat{wm}_i). \quad (9)$$

B.2. TPR@FPR

We report TPR@FPR for detection purpose, where we introduce a threshold $\tau \in [0, 1]$ on the bit accuracy. An image is classified as watermarked if $Acc(wm, \hat{wm}) > \tau$. Different choices of τ lead to different true positive rates (TPR) and false positive rates (FPR).

In diffusion watermarking, we typically cannot directly measure the FPR, because we only observe positive (watermarked) samples in practice. Following GS [49], for negative (non-watermarked) samples, we assume that their extracted watermark bits $\hat{wm}_1, \hat{wm}_2, \dots, \hat{wm}_k$ are independently and identically distributed, where each bit follows a Bernoulli distribution $Ber(0.5)$. Under this assumption, the bit accuracy of negative (non-watermarked) samples follows a binomial distribution $B(k, 0.5)$. Therefore, we can

use the binomial distribution to approximate the FPR as

$$\begin{aligned} FPR(\tau) &= \mathbb{P}(Acc(wm, \hat{wm}) > \tau) \\ &= \frac{1}{2^k} \sum_{i=\tau+1}^k \binom{k}{i} \\ &= \beta_{1/2}(\tau + 1, k - \tau), \end{aligned} \quad (10)$$

where $\beta_{1/2}(\cdot, \cdot)$ is a regularized incomplete beta function.

Finally, we compute TPR@FPR as follows: 1) Choose the desired FPR. 2) Solve Eq. (10) to obtain the corresponding threshold τ . 3) Evaluate the proportion of watermarked images whose bit accuracies exceed the threshold τ , which corresponds to the empirical TPR, defined as

$$TPR = \frac{1}{N} \sum_i^N \mathbf{1}(Acc(wm_i, \hat{wm}_i) > \tau). \quad (11)$$

In our experiments, we fix FPR=1e-6. The resulting thresholds τ for all f_{hw} configurations are listed in Tab. 12 (noted that $k = \frac{c \cdot h \cdot w}{f_{hw}^2}$).

Table 12. Threshold τ for different f_{hw} with FPR=1e-6.

f_{hw}	1	2	4	8
τ	0.5186	0.5371	0.5742	0.6484

With the above construction, TPR@FPR=1e-6 is computed by thresholding bit accuracy and is therefore a monotonic function of bit accuracy. Consequently, we adopt bit accuracy as our primary evaluation metric and report it in all related tables, while TPR@FPR=1e-6 is only included in Tab. 1 for reference.

Moreover, to complement this single operating point (FPR=1e-6) and provide a more comprehensive comparison, we further sweep the FPR over a logarithmic grid and compute the Area Under the Receiver Operating Characteristic Curve (AUC-ROC) [4], as detailed in Sec. C.1.

C. Robustness Evaluation

In this section, we provide additional details on the robustness evaluation of OSI.

C.1. Image Distortion

We adopt nine types of adversarial image distortions to evaluate the robustness of OSI method, as illustrated in Fig. 5.

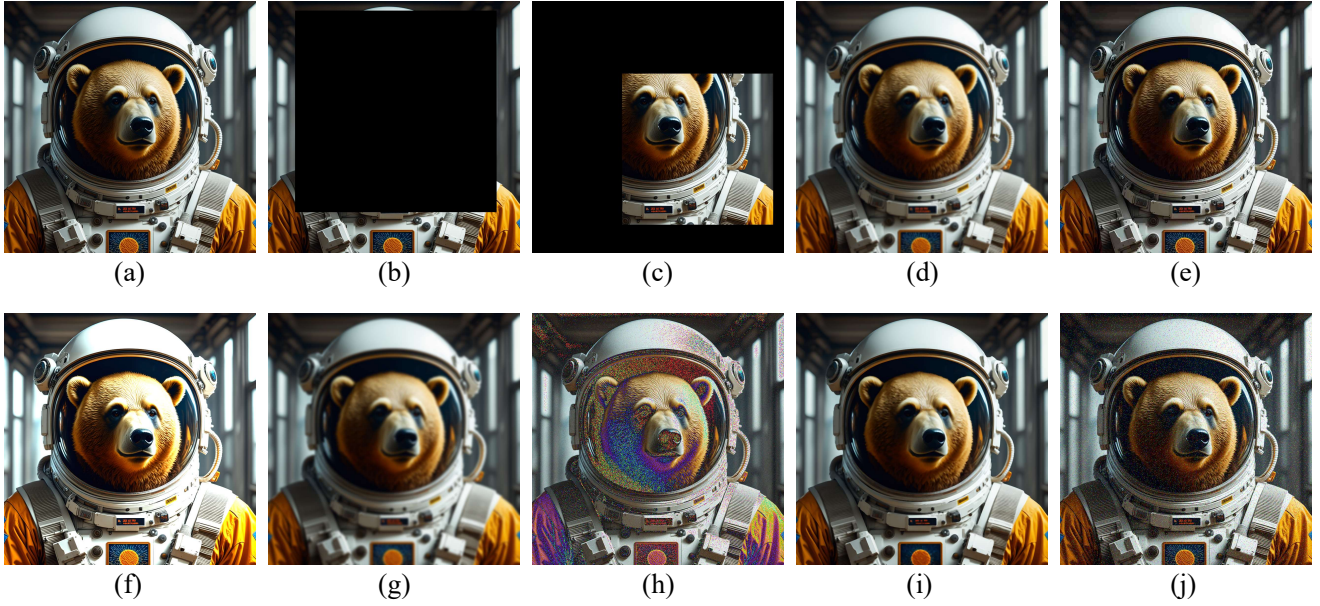


Figure 5. Visualization of different adversarial image distortions. (a) Clean watermarked image. (b). 80% random drop. (c) 60% random crop. (d) Resize to 25% and restore. (e) JPEG with $QF = 25$. (f) Brightness with $f = 6$. (g) Gaussian blur with $r = 4$. (h) Gaussian Noise with $\mu = 0, \sigma = 0.05$. (i) Median blur with $k = 7$. (j) Salt & Pepper noise with $p = 0.05$.

Table 13. Bit accuracy comparisons among all adversarial scenarios with GS [49] on SD2.1.

Method	f_{hw}	Clean	RandDrop	RandCrop	Resize	JPEG	Bright	GausBlur	GausStd	MedBlur	SPNoise	Adv. Avg
GS	1	0.8560	0.6156	0.6187	0.7050	0.6885	0.6951	0.6516	0.6389	0.7254	0.6151	0.6616
	2	0.9408	0.6703	0.6761	0.7883	0.7671	0.7634	0.7195	0.7015	0.8135	0.6683	0.7298
	4	0.9984	0.8223	0.8338	0.9464	0.9200	0.8828	0.8821	0.8462	0.9630	0.8089	0.8784
	8	1.0000	0.9651	0.9747	0.9972	0.9878	0.9538	0.9849	0.9567	0.9988	0.9365	0.9728
OSI (ours)	1	0.8839	0.6444	0.6428	0.7576	0.7351	0.7220	0.7227	0.7589	0.7822	0.8622	0.7364
	2	0.9607	0.7111	0.7091	0.8501	0.8238	0.7926	0.8105	0.8509	0.8764	0.9453	0.8189
	4	0.9996	0.8841	0.8801	0.9815	0.9617	0.9081	0.9632	0.9752	0.9892	0.9986	0.9491
	8	1.0000	0.9899	0.9921	0.9997	0.9971	0.9685	0.9992	0.9987	0.9998	1.0000	0.9939

Table 14. TPR@FPR=1e-6 comparisons among all adversarial scenarios with GS [49] on SD2.1.

Method	f_{hw}	Clean	RandDrop	RandCrop	Resize	JPEG	Bright	GausBlur	GausStd	MedBlur	SPNoise	Adv. Avg
GS	1	1.0000	1.0000	1.0000	1.0000	0.9990	0.9890	1.0000	0.9970	1.0000	0.9990	0.9982
	2	1.0000	1.0000	1.0000	1.0000	0.9990	0.9810	1.0000	0.9920	1.0000	0.9980	0.9967
	4	1.0000	0.9990	1.0000	1.0000	1.0000	0.9770	1.0000	0.9930	1.0000	0.9990	0.9964
	8	1.0000	1.0000	1.0000	1.0000	1.0000	0.9810	1.0000	0.9930	1.0000	0.9990	0.9970
OSI (ours)	1	1.0000	1.0000	1.0000	1.0000	1.0000	0.9920	1.0000	1.0000	1.0000	1.0000	0.9991
	2	1.0000	1.0000	1.0000	1.0000	1.0000	0.9860	1.0000	1.0000	1.0000	1.0000	0.9984
	4	1.0000	1.0000	1.0000	1.0000	1.0000	0.9870	1.0000	1.0000	1.0000	1.0000	0.9986
	8	1.0000	1.0000	1.0000	1.0000	1.0000	0.9860	1.0000	1.0000	1.0000	1.0000	0.9984

Table 15. Bit accuracy comparisons among all adversarial scenarios with GS [49] on SDXL.

Method	f_{hw}	Clean	RandDrop	RandCrop	Resize	JPEG	Bright	GausBlur	GausStd	MedBlur	SPNoise	Adv. Avg
GS	1	0.7845	0.5935	0.5993	0.6388	0.6195	0.6326	0.5904	0.6098	0.6572	0.5698	0.6123
	2	0.8789	0.6388	0.6477	0.7027	0.6768	0.6879	0.6340	0.6631	0.7282	0.6049	0.6649
	4	0.9894	0.7719	0.7878	0.8609	0.8238	0.8016	0.7579	0.8034	0.8918	0.7079	0.8008
	8	0.9999	0.9267	0.9452	0.9772	0.9523	0.8908	0.9040	0.9400	0.9883	0.8500	0.9305
OSI (ours)	1	0.8276	0.6154	0.6185	0.6883	0.6595	0.6598	0.6523	0.6717	0.7041	0.7383	0.6676
	2	0.9185	0.6708	0.6751	0.7687	0.7319	0.7218	0.7210	0.7479	0.7889	0.8294	0.7395
	4	0.9963	0.8237	0.8314	0.9318	0.8936	0.8345	0.8818	0.9096	0.9475	0.9689	0.8914
	8	1.0000	0.9646	0.9741	0.9967	0.9864	0.9150	0.9861	0.9907	0.9982	0.9990	0.9790

Table 16. Bit accuracy comparisons among all adversarial scenarios with GS [49] on SD3.5.

Method	f_{hw}	Clean	RandDrop	RandCrop	Resize	JPEG	Bright	GausBlur	GausStd	MedBlur	SPNoise	Adv. Avg
GS	1	0.7604	0.5850	0.5953	0.5800	0.5759	0.6572	0.5541	0.5424	0.5896	0.5499	0.5810
	2	0.8520	0.6269	0.6424	0.6183	0.6136	0.7244	0.5806	0.5632	0.6330	0.5749	0.6197
	4	0.9746	0.7489	0.7770	0.7314	0.7220	0.8698	0.6640	0.6270	0.7581	0.6518	0.7278
	8	0.9982	0.8942	0.9335	0.8722	0.8588	0.9635	0.7919	0.7246	0.9051	0.7713	0.8572
OSI (ours)	1	0.7978	0.5993	0.6087	0.6213	0.6065	0.6818	0.5982	0.6282	0.6434	0.7252	0.6347
	2	0.8887	0.6468	0.6611	0.6773	0.6562	0.7520	0.6449	0.6859	0.7082	0.8092	0.6935
	4	0.9858	0.7812	0.8068	0.8243	0.7923	0.8940	0.7774	0.8323	0.8666	0.9478	0.8359
	8	0.9993	0.9275	0.9569	0.9572	0.9283	0.9732	0.9281	0.9521	0.9786	0.9941	0.9551

Table 17. Bit accuracy comparisons among all adversarial scenarios with PRCW [15] on SD2.1.

Method	Msg. Bit	Clean	RandDrop	RandCrop	Resize	JPEG	Bright	GausBlur	GausStd	MedBlur	SPNoise	Adv. Avg
PRC	4096	0.8751	0.8752	0.8751	0.8752	0.8750	0.8750	0.8751	0.8750	0.8748	0.8754	0.8751
	2048	0.9480	0.9376	0.9375	0.9374	0.9375	0.9387	0.9374	0.9376	0.9374	0.9374	0.9376
	1024	1.0000	0.9688	0.9687	0.9775	0.9778	0.9801	0.9687	0.9696	0.9848	0.9691	0.9739
	512	1.0000	0.9847	0.9855	0.9975	0.9930	0.9929	0.9872	0.9872	0.9983	0.9860	0.9903
	256	1.0000	0.9969	0.9980	0.9997	0.9982	0.9970	0.9964	0.9950	0.9997	0.9934	0.9972
OSI (ours)	4096	0.8752	0.8753	0.8751	0.8752	0.8750	0.8752	0.8750	0.8749	0.8747	0.8752	0.8751
	2048	0.9605	0.9374	0.9375	0.9374	0.9374	0.9399	0.9375	0.9387	0.9377	0.9518	0.9395
	1024	1.0000	0.9878	0.9878	0.9966	0.9913	0.9856	0.9881	0.9965	0.9984	1.0000	0.9925
	512	1.0000	1.0000	0.9998	0.9998	0.9994	0.9958	0.9994	0.9995	0.9998	1.0000	0.9993
	256	1.0000	0.9998	0.9999	1.0000	0.9997	0.9980	0.9999	0.9998	1.0000	1.0000	0.9997

Table 18. Bit accuracy comparisons among all adversarial scenarios with T2SMark [48] on SD2.1.

Method	Msg. Bit	Clean	RandDrop	RandCrop	Resize	JPEG	Bright	GausBlur	GausStd	MedBlur	SPNoise	Adv. Avg
T2S	4096	0.9909	0.7204	0.7294	0.8819	0.8429	0.8262	0.8078	0.7562	0.9031	0.7261	0.7993
	2048	0.9979	0.7991	0.7784	0.9481	0.9083	0.8776	0.8875	0.8180	0.9612	0.7931	0.8635
	1024	0.9998	0.9073	0.9575	0.9863	0.9628	0.9341	0.9542	0.8871	0.9912	0.8677	0.9387
	512	1.0000	0.9792	0.9915	0.9974	0.9892	0.9661	0.9881	0.9401	0.9987	0.9304	0.9756
	256	1.0000	0.9984	0.9992	0.9995	0.9967	0.9807	0.9982	0.9748	0.9998	0.9704	0.9909
OSI (ours)	4096	0.9977	0.7626	0.7642	0.9455	0.9137	0.8616	0.9132	0.9338	0.9611	0.9929	0.8943
	2048	0.9998	0.8527	0.8119	0.9863	0.9657	0.9122	0.9713	0.9762	0.9916	0.9986	0.9407
	1024	1.0000	0.9595	0.9891	0.9985	0.9936	0.9638	0.9958	0.9963	0.9992	0.9999	0.9884
	512	1.0000	0.9988	0.9996	0.9999	0.9993	0.9854	0.9997	0.9997	1.0000	1.0000	0.9980
	256	1.0000	1.0000	1.0000	1.0000	0.9998	0.9920	1.0000	0.9999	1.0000	1.0000	0.9991

The average performance over all adversarial settings has already been summarized in Tab. 1, Tab. 7 and Tab. 8 of the main paper. Here, we further present per-distortion results to offer a more fine-grained analysis. Specifically, we report the bit accuracy under each distortion in Tab. 13, Tab. 15 and Tab. 16, corresponding to SD2.1, SDXL and SD3.5 diffusion models, respectively. For SD2.1, we additionally provide per-distortion TPR@FPR=1e-6 in Tab. 14. These detailed results consistently show that OSI outperforms the GS baseline across all considered distortion types and diffusion backbones.

We also compare OSI with PRCW [15] in Tab. 17, where we report the per-distortion bit accuracy. Although OSI is slightly inferior to PRCW under a few specific distortion settings, it still achieves better overall robustness while requiring only a single inversion step. In addition, Tab. 18 presents per-distortion bit accuracy for T2SMMark [48]. Across all distortion scenarios, OSI consistently surpasses the original T2SMMark.

To obtain an integrated measure that jointly accounts for true positive rate (TPR) and false positive rate (FPR), we further report logAUC. Concretely, we scan the FPR on a logarithmic scale from 10^{-12} to 10^{-1} and compute the area under the resulting ROC curve. The visualization in Fig. 6 shows that our OSI method consistently outperforms GS in logAUC across all f_{hw} configurations and adversarial scenarios, further demonstrating the superiority of OSI.

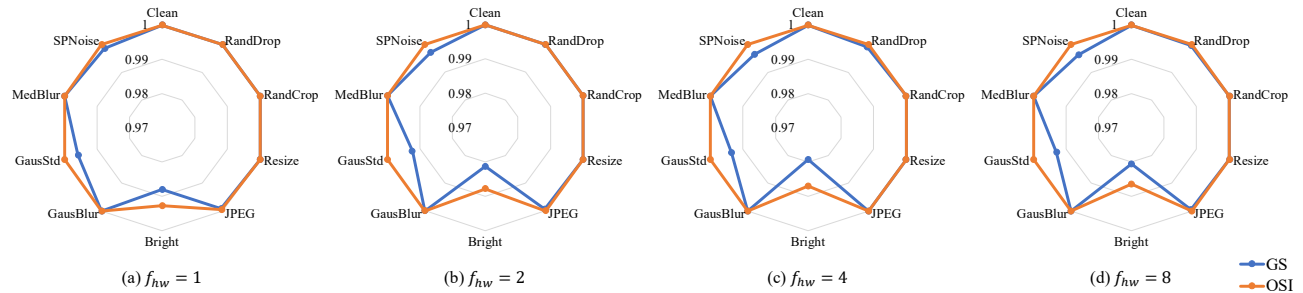


Figure 6. LogAUC values of GS and OSI under different f_{hw} settings across various image distortions.

Table 19. Bit accuracy comparisons under advanced attacks on SD2.1.

Method	f_{hw}	Compression						Embedding	
		bmshj_factorized	bmshj_hyperprior	mbt2018_mean	mbt2018	cheng_anchor	cheng_attn	CLIP	ResNet18
GS	1	0.6165	0.6222	0.6219	0.6276	0.6314	0.6321	0.6384	0.6403
	2	0.6707	0.6776	0.6775	0.6853	0.6904	0.6917	0.6992	0.7014
	4	0.8120	0.8194	0.8204	0.8313	0.8370	0.8381	0.8568	0.8601
	8	0.9409	0.9406	0.9404	0.9498	0.9524	0.9519	0.9640	0.9653
OSI (ours)	1	0.6241	0.6302	0.6310	0.6344	0.6413	0.6423	0.6513	0.6543
	2	0.6814	0.6887	0.6901	0.6947	0.7040	0.7058	0.7171	0.7205
	4	0.8279	0.8360	0.8375	0.8442	0.8560	0.8586	0.8783	0.8824
	8	0.9528	0.9528	0.9550	0.9590	0.9651	0.9656	0.9749	0.9766

and then seek an adversarial image I_{adv} that is close to I in pixel space but yields a substantially different embedding $f(I_{adv})$. Formally, the objective is defined as:

$$\max_{I_{adv}} \mathbf{Dist}(f(I_{adv}), f(I)) \quad \text{s.t.} \quad \|I_{adv} - I\|_\infty \leq \delta, \quad (13)$$

where \mathbf{Dist} denotes a distance measure, and δ is the perturbation budget controlling the maximum allowable pixel-wise deviation. After optimizing Eq. (13), I_{adv} is likely to induce failure in watermark extraction. In our experiment, we instantiate embedding attack using two encoders, ResNet-18 [17] and CLIP [39]. As shown in Tab. 19, OSI still outperforms GS across all settings.

D. Additional Studies

D.1. Step-wise Bit Accuracy

In this part, we present a comprehensive analysis of the step-wise bit accuracy for GS, using latents at each step of the multi-step diffusion inversion process for watermark verification. For the 50-step inversion setting, we denote the latent from the encoder output as Step-0 and the latent after the final inversion step as Step-50.

In Fig. 7(a), we report the watermark $(\frac{c \cdot h \cdot w}{f_{hw}^2})$ bit accuracy in the clean scenario. For all f_{hw} configurations, the watermark bit accuracy increases steadily as the inversion step index grows. Larger f_{hw} leads to higher accuracy. In

particular, even the encoder output Step-0 already achieves over 98% bit accuracy when $f_{hw} = 8$. These observations confirm the inherent inversion capability of both the diffusion backbone and the encoder.

In Fig. 7(b), we directly evaluate the bit accuracy at the latent level $(c \cdot h \cdot w)$. The resulting curves for different f_{hw} are highly similar, indicating that REP does not change the intrinsic inversion capability of the model. Instead, REP primarily provides gains at the cryptographic procedure by adding redundancy to the watermark bits. As discussed in Sec. 4, the similarity in Fig. 7(b) indicates that different codings (f_{hw}) do not change the channel capacity (latent bit accuracy). Moreover, this similarity also explains why we conduct several ablation studies with a fixed setting $f_{hw} = 1$ (see Tab. 5, Tab. 6 and Tab. 9), since varying f_{hw} does not qualitatively affect the underlying inversion behavior.

D.2. Different Cryptographic Modules

GS [49] provides two different cryptographic modules, ChaCha20 [3] and a simple XOR-based scheme, for encrypting repeated watermarks into sign masks and decrypting them back. We conduct an ablation study to compare their impact on overall watermarking performance. As shown in Tab. 20, the results obtained with them are almost identical, with no meaningful performance gap. This observation is consistent with our communication system per-

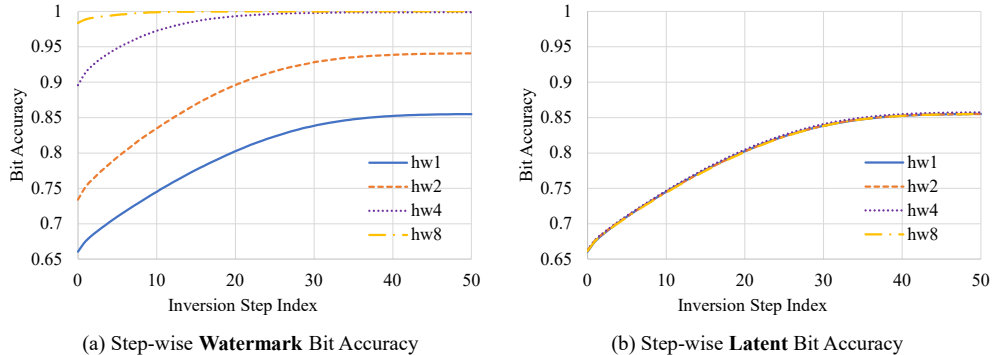


Figure 7. Step-wise Accuracy across different f_{hw} configurations for GS [49]. Watermark bit accuracy is calculated by evaluating the recovery of the watermark $(\frac{c \cdot h \cdot w}{f_{hw}^2})$. Latent bit accuracy is calculated by evaluating the recovery of the initial latent $(c \cdot h \cdot w)$.

Table 20. Comparisons among different cryptographic modules for GS.

Method	Module	Clean				Adversarial			
		1	2	4	8	1	2	4	8
GS	ChaCha20	0.8552	0.9416	0.9984	1.0000	0.6613	0.7286	0.8786	0.9724
	XOR	0.8560	0.9408	0.9984	1.0000	0.6616	0.7298	0.8784	0.9728
OSI	ChaCha20	0.8839	0.9607	0.9996	1.0000	0.7364	0.8189	0.9491	0.9939
	XOR	0.8841	0.9607	0.9996	1.0000	0.7364	0.8179	0.9490	0.9941

Table 21. Comparison among different total inversion steps.

	GS								OSI
	1	10	20	30	40	50	100		
Clean	0.7241	0.8260	0.8433	0.8500	0.8538	0.8560	0.8604	0.8839	
Adversarial	0.5968	0.6116	0.6139	0.6146	0.6149	0.6151	0.6155	0.7364	

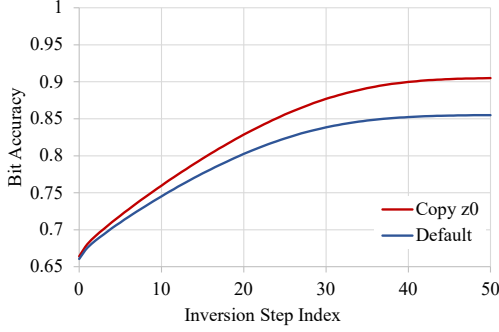


Figure 8. Effect of copying z_0 for multi-step diffusion inversion.

spective in Sec. 4, where we disentangle coding from the channel. The designs of coding do not affect the underlying channel capacity.

D.3. Different Total Inversion Steps

In Sec. D.1, we analyze the performance of the latents at each step of a 50-step diffusion inversion process. Here, we further investigate how the total number of inversion steps affects watermark extraction using GS. As shown in Tab. 21, increasing the total number of inversion steps generally leads to higher bit accuracy. However, the gains quickly saturate, with additional steps yielding only marginal benefits. Notably, OSI demonstrates superior performance compared to the computationally intensive 100-step inversion, despite requiring only a single forward step, which further demonstrates both the effectiveness and efficiency of OSI.

D.4. Alignment of Encoder Output

In Sec. 3.2, we introduce \mathcal{L}_{MSE} to align the encoder output latent \hat{z}_0 during watermark extraction and decoder input latent z_0 during image generation. This alignment improves the overall watermark extraction performance, as evidenced by the ablation results in Tab. 4. Here we provide a complementary experiment based on GS. Specifically, during watermark extraction, we directly replace \hat{z}_0 with z_0 and evaluate the corresponding step-wise bit accuracy. As shown in Fig. 8, the bit accuracy increases after the replacement, indicating that better alignment between \hat{z}_0 and z_0 is crucial for achieving higher extraction accuracy. From a communication system perspective, this alignment can be interpreted as a partial improvement of the effective channel, which can

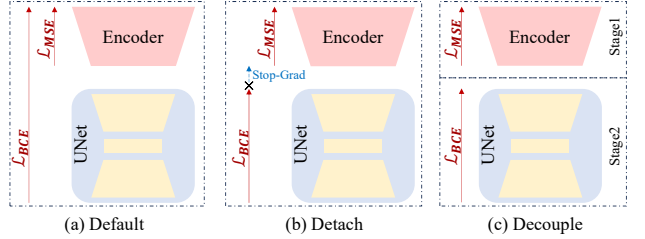


Figure 9. Visualization of 3 finetuning strategies.

Table 22. Comparison of finetuning strategies.

	Default	Detach	Decouple
Clean	0.8839	0.8714	0.8725
Adversarial	0.7364	0.7227	0.7231

be schematically represented as

$$wm \rightarrow \dots \rightarrow z_0 \rightarrow \hat{z}_0 \rightarrow \dots \rightarrow \hat{wm}. \quad (14)$$

By reducing the noise introduced during the decoding–encoding transition ($z_0 \rightarrow \hat{z}_0$), the alignment improves the overall channel capacity. Consequently, we explicitly enforce this alignment during finetuning to further improve the effective capacity of our OSI model.

D.5. Different Finetuning Strategy

In this section, we describe the finetuning strategies used for OSI. We introduce \mathcal{L}_{BCE} and \mathcal{L}_{MSE} to supervise the finetuning of OSI. The \mathcal{L}_{MSE} term is back-propagated only through the encoder, whereas the \mathcal{L}_{BCE} term can be applied under different strategies. By default, we use \mathcal{L}_{BCE} to jointly update both the UNet and the encoder. In addition, we investigate two variants where only the UNet is updated by \mathcal{L}_{BCE} . The first variant, denoted “detach”, performs end-to-end finetuning but detaches the gradient between the UNet and the encoder, so that \mathcal{L}_{BCE} does not update the encoder parameters. The second variant, denoted “decouple”, adopts a two-stage procedure: in stage 1, we finetune the encoder using \mathcal{L}_{MSE} ; in stage 2, we freeze the encoder and finetune only the UNet using \mathcal{L}_{BCE} . We illustrate all three strategies in Fig. 9. As summarized in Tab. 22, our default finetuning strategy consistently outperforms both “detach” and “decouple”, and is thus used in all main experiments.